Gasoline Particulate Filter wall permeability testing

Aleksandrova, S., Saul, J., Medina, H., Garcia-Afonso, O., Lin, C., Herreros, J. M., Bevan, M. & Benjamin, S

ESSN 1946-3944
Publisher: SAE International

20XX-01-XXXX

Gasoline Particulate Filter wall permeability testing

Author, co-author (Do NOT enter this information. It will be pulled from participant tab in MyTechZone)

Affiliation (Do NOT enter this information. It will be pulled from participant tab in MyTechZone)

ABSTRACT

With the introduction of particulate matter emissions regulations for gasoline engines, most car manufacturers are considering using Gasoline Particulate Filters (GPF). Although very similar to Diesel Particulate Filters (DPF), GPFs operate at higher temperatures and generally have thinner monolith walls. In order to estimate the pressure loss through the filter, filter wall permeability is needed. This presents a number of challenges since wall losses cannot be efficiently isolated from other losses in a full scale filter or filter core. Thin wall wafers have been used for DPF characterisation. However, GPF wafers are generally thinner, which makes the testing less straightforward. This paper presents a novel effective methodology for estimation of GPF wall permeability using thin wafers cut from the filter monolith. Both cold and hot flow permeability can be estimated, which allows to account for the change of apparent permeability due to the slip effect. The flow through the wafer is also modelled numerically to assess the effect of the uneven wafer surface resulting from wafer preparation method. A technique for calculating corrected permeability is suggested which is estimated to provide values within 5% of the "nominal" value. Combining experimental results with the applied correction, consistent permeability values have been obtained for seven wafer samples. Maximum variation in the permeability values was 10%, with a standard error of ±2.5% of the mean. Being able to assess filter wall permeability from a simple cold flow pressure testing procedure will allow development of more efficient flow and pressure loss models for Gasoline Particulate Filters, which in turn will facilitate design of efficient aftertreatment systems with lower back pressure.

INTRODUCTION

Gasoline emissions control catalysis has been around for more than 30 years [1]. However, the stringent Euro 6 emissions standards resulted in an increased interest in GPF (Gasoline Particular Filter) technology. Although the wall-flow filter geometry is similar to Diesel Particulate Filter (DPF) and Selective Catalyst Reduction Filter (SCRF) geometries, there are differences in structure, operating conditions (mass flow rates, temperatures, regeneration regime [2]) and wall properties (thickness, porosity, pore size). Therefore, separate studies of GPF pressure losses and flow uniformity are needed to improve predictions offered by existing DPF/SCRF research, and to provide adequate models for CAE analysis.

Various models have been developed for modelling the flow and pressure losses in wall-flow particulate filters. The most popular one-dimensional model is based on the study by Bissett [3] which was further developed and validated by Konstandopolous and others (e.g. [4], [5], [6], [7], [8], [9]) to account for soot loading, transient conditions, slip effect etc. The model assumes one-dimensional unidirectional flow inside the inlet and outlet channels with wall velocity perpendicular to the channels. The resulting equations are solved analytically. Other models include the two-dimensional model by Opris et al ([10], [11]), and the one-dimensional model by Oxarango [12]. Unlike the Bisset model, however, the other models do not provide a ready analytical expression necessary for practical applications.

There are several sources of filter pressure loss, including contraction/expansion losses, friction losses and through wall losses [7]. Through wall losses are arguably the best defined out of the above, as they are well described by Darcy law, with the non-linear Forcheimer contribution to have been shown to be negligible in multiple studies (e.g. [6]). However, correct evaluation of Darcy losses relies heavily on the value of porous wall permeability. Therefore, a great deal of research has been carried out on different methods of permeability estimation. These include empirical expressions based on the wall porosity and pore size and distribution (e.g. [13], [14]), and calculating permeability from experiments (see e.g. [2], [7], [8], [15], [16]). Comprehensive reviews of available models and pressure loss descriptors are available in literature (for example, [16]), and therefore not discussed here.

Most experimental techniques involve measurement of cold flow pressure losses for different wall flow velocities, followed by calculation of the permeability based on the analysis presented in [4] or more refined one-dimensional models. This approach is based on several assumptions, namely that the flow rate is equal in all channels, the friction losses are equal to those predicted by the one-dimensional flow model, and that the local friction coefficient does not vary with the wall suction/injection Reynolds number. These assumptions have been shown to produce good results in several experimental studies ([7], [8], [15]). However, it is expected that in

GPFs due to higher flow rates wall suction/injection effect becomes more important and changes friction loss parameters. Moreover, it has been recently shown [15] that the one-dimensional model used by a multitude of authors does not take into account tangential transport of axial momentum, and thus an important part of the momentum transfer physics is not accounted for. In most published experimental studies, these differences are not very large and the missing/underestimated terms are balanced by lower effective permeability values obtained from the fitting of the calibration curves. For higher flow rates and temperatures these discrepancies become more important, so that the model cannot be easily applied to higher mass flow rates and temperatures than those calibrated for.

To eliminate the uncertainty associated with estimating losses from friction, expansion and contraction, several authors used wafer samples ([2], [17], [18], [21]). Lambert et al [2] quote permeability values derived from wafer testing, with wafers obtained from filter monoliths. However, no details of sample preparation and quality, error/variability estimates or description of the experiments are provided. Viswanathan et al [17] quote permeability values obtained from wafer testing with remarkable accuracy (< 2%). The authors refer the reader to work by Wirojsakunchai et al [18] for details of the experimental setup, where much higher experimental errors are shown, and the pressure loss variation between two wafers of the same specification appears to exceed 15%. However, the improvements that Viswanathan et al [17] have achieved for increased result accuracy compared to the work of Wirojsakunchai et al [18] are not documented. Kamp et al [21] present a thorough experimental programme which includes multilayer wafer permeability measurement. The resulting values have a very high repeatability (< 2% standard deviation for unloaded wafers). However, any surface defects on the DPF wafer samples have been removed by sanding which was impossible to do on much thinner and very fragile GPF wafers used in current study. Other authors ([19], [20]) used wafer samples to investigate filtration and thermal properties of monoliths. In a carefully conducted experiment with a uniform sample of uniform thickness with uniform inlet flow, the only pressure loss comes from Darcy losses, allowing the calculation of the permeability with a reasonable degree of accuracy. Although promising, most of these studies do not describe sample source or preparation. Moreover, all of these studies have been performed for cold flow only, despite the fact that the slip effect becomes important for high flow temperatures [5] and no truly predictive model for slip effect evaluation exists.

In this study, we demonstrate a novel experimental technique to measure both cold and hot flow permeability. The sample preparation is described in detail, and a correction for permeability values is suggested to account for the fact the cut wafers are not completely flat. The hot flow results are analysed to characterise the importance of the slip effect, and different existing slip flow models are assessed.

EXPERIMENTAL SETUP

Test samples

Single wafer test samples were cut from the same bare 300/8 GPF monolith using a piercing saw (Figure 1). An extractor fan was used to ensure that the dust from cutting was removed and did not block the sample pores. Care was taken to make the sample surface as flat as possible, however remains of the side walls ("ridges") were still present on most samples (Figure 2). Due to wafer fragility it was not possible to remove these ridges. Therefore, a correction was applied to account for the thicker ridges when estimating permeability as discussed later in this paper. The average ridge height was estimated to be between 1 and 2 wall thickness values.

In order to hold the fragile samples in place and eliminate leaks, the rectangular wafer samples were sealed in the holders using a high-temperature silicone sealer as illustrated in Figure 3. The diameter of the open section of the holder presented to the flow was 50 mm. Although it was not possible to directly check for leaks around the wafer sample edges, hot wire measurements downstream of the wafers did not show any evidence of higher velocities near the edges. Inspection of the wafer sample edges after testing also showed good sealing that would block any flow (apart from the wafers after highest temperature tests where the sealant disintegrated resulting in wafer fracture). For those samples that did not fracture at higher temperatures, cold flow tests were repeated after the hot flow testing. The repeatability was within the experimental error, which confirms that there were no leaks caused by part movement/expansion at higher temperatures. When wafer failure did occur, the pressure trend immediately deviated from linear, and these test results were discarded.

Different materials were explored for both wafer holders and the sealant. There was no difference observed in test results and wafer failure rate between different high temperature gasket materials and stainless steel holders. Klinger Milam gasket material was finally chosen because such holders were disposable, and multiple samples could be prepared for testing at once. Several cement-based and silicone-based sealants were tested to find the most suitable material

Figure 1 A wafer sample

Figure 2 A single wafer sample in the holder

(a)

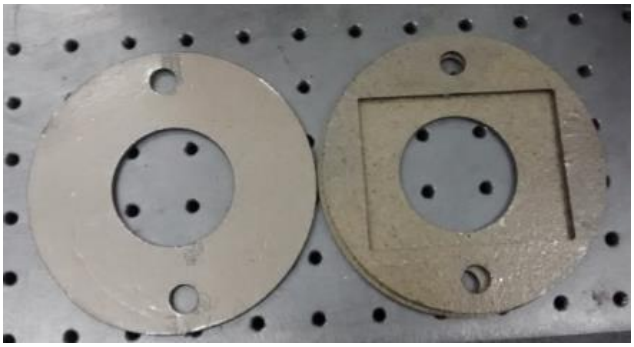

(b)

Figure 3 Sample holder from high temperature gasket material (a) and the process of sealing the sample with silicone sealer (b)

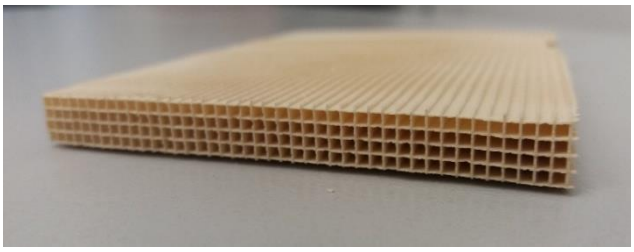

Figure 4 A multiple layer sample

for securing wafers in the holders. Inflexible sealants (fire cements and similar) proved to be unsuitable as wafers often fractured during the drying/curing process. Envirograf Heat-Resistant Silicone Sealant was chosen as it retained flexibility even when cured (24 hour curing period was used for all samples).

Multiple samples have been tested to ensure test repeatability. It was not possible to repeat the tests with the same sample as the mass flow rate in most cases was increased to the point of wafer mechanical failure.

Multilayer wafers have been used before for filter property evaluation [20, 21]. Such samples are easier to cut and better cut quality can be achieved (Figure 4). Two samples have been tested to evaluate the potential of using multiple layers for wafer permeability evaluation. These were cut in similar manner from a different monolith with the same specification.

An attempt has also been made to use single catalysed wafer samples, prepared in the same way as uncoated samples as discussed above. The samples had high washcoat loading typical for production catalysts. However, the coating of the filters used in this study varied not only between different parts of the filter, but even in adjacent channels. Thus, wall thickness varied between different samples and in different parts of any single sample. It will be shown that large coating variation between samples makes a consistent analysis impossible.

Hot flow rig

The pressure drop across the wafers was measured on a 36 kW hot flow rig. The flow rig design (Figure 5) includes the following components: Compressed air from a compressor supplies a Sylvania SureMax heater (2). Since the minimum mass flow rate safety requirement for the heater is 6 g/s, part of the flow had to be diverted downstream of the heater to achieve the required, much lower mass flow rates. This was achieved using a Y-piece (3) and a bleed valve (4). The upstream instrumentation section (5) contains a flow straightener (a 30 mm long section of bare catalyst monolith), 4 pressure tappings and a thermocouple access point. Downstream of the test section (6) a 402 mm long outlet sleeve (7) is attached with

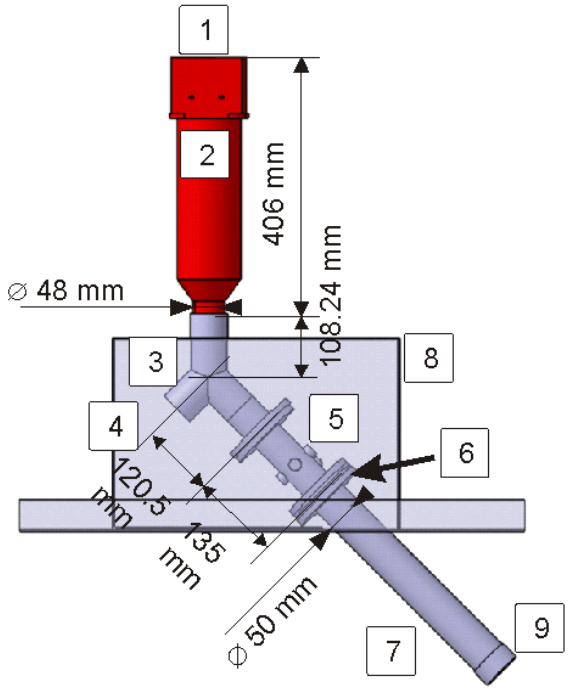

Figure 5 Hot flow rig

Figure 6 Pitot tube position at the outlet of the orifice plate

an orifice plate (9) used for mass flow rate measurements with a Pitot tube. Most of the rig is contained within a "heat shield" (8) - a stainless steel plenum designed to use the discarded hot air from the valve (4) to ensure that the test section reaches the thermal equilibrium quickly. The whole rig including the heater and inside and outside of the heat shield was insulated using several layers of ceramic fibre blanket. The test section was considered to be in the thermal equilibrium state when the upstream and downstream gas temperatures changed by less than ±1K in 5 minutes.

In order to estimate the wafer resistance, the flow through the test section has to be as uniform as possible. Although presenting air flow with high resistance usually results in flattening of the velocity profile, the flow uniformity downstream of the test section was checked using Hot Wire Anemometry. The resulting velocity profile 3 mm downstream of the wafer sample remained uniform within 5% for the whole range of mass flow rates considered here.

Experimental procedure

Upstream and downstream pressure and temperatures, as well as pressure and temperature readings from the Pitot tube were logged using a bespoke LabView interface at time intervals of approximately 0.5 s. The total mass flow rate supplied to the heater at point (1) was adjusted using a calibrated Viscous Flow Meter (VFM). The actual (diverted) mass flow rate through the test section was calculated in real time from Pitot tube pressure and temperature readings. A digital micromanometer was used for Pitot tube differential pressure measurements, with the accuracy of ± (0.25% of reading + 0.001 Pa). The largest mass flow measurement error contribution came from the Viscous Flow Meter readings which have 3-4% uncertainty at mass flow rates up to 10 g/s. The wafer back pressure was recorded using a digital manometer with an accuracy of ± 6 Pa in the relevant range. Each measurement was averaged from 10 consecutive readings, and the variation between these did not exceed 1%.

For the hot flow tests, the maximum mass flow rates did not exceed 0.5 g/s, with mean velocities of up to around 0.6 m/s. For a clean 300/8 filter with diameter 0.12 m and length 0.1 m this corresponds to around 2000 kg/hr at a temperature of 700°C. These values are much higher than typical exhaust mass flows, however through wall flow in filters is not uniform, and the mean wall flow velocity will vary with filter size, therefore information about losses at higher flow velocities can also be valuable. Measurements of flow velocities were achieved by accelerating the flow using an orifice plate with a 12 mm diameter orifice. A 6 mm Pitot tube was attached securely to the orifice plate as shown in Figure 6.

For each set of tests, the Pitot tube was calibrated in cold flow conditions with the bleed valve fully closed. With the mass flow rate known from VFM readings, it was assumed that

$$\dot{m}_{VFM} = K_d \dot{m}_{Pitot} . \quad (1)$$

Here $\dot{m}_{VFM}$ is the actual mass flow rate set using the VFM, $\dot{m}_{Pitot}$ is the mass flow rate calculated from Pitot tube readings and K_d is the orifice plate discharge coefficient. The discharge coefficient was calculated using linear regression on a set of measurements for around 10 different mass flow rates. Values of discharge coefficient varied slightly depending on the Pitot tube position, and recalibration was carried out if the Pitot tube needed to be moved. A temperature correction was applied.

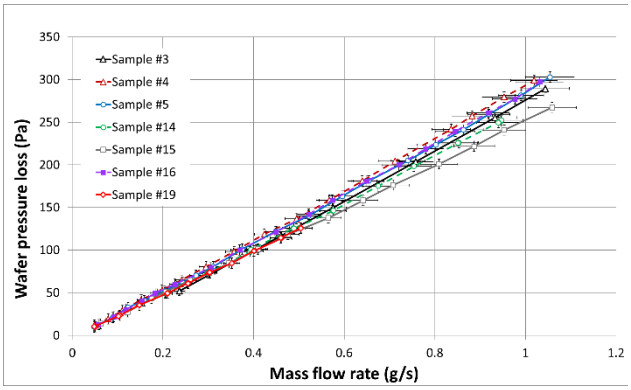

Figure 7 Pressure loss versus mass flow rate for bare wafers, cold flow

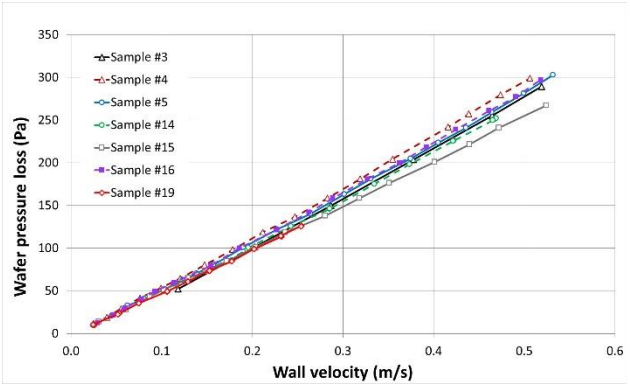

Figure 8 Pressure loss versus mean wall velocity for bare wafers, cold flow

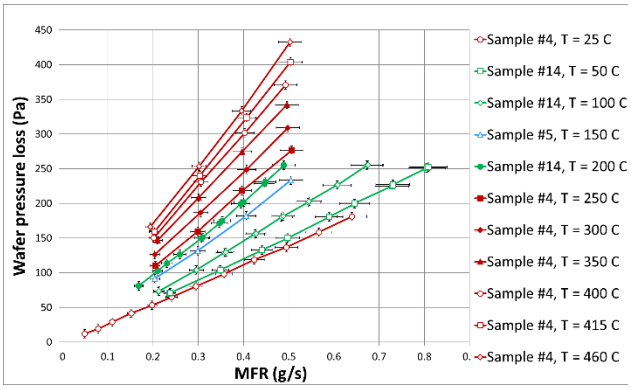

Figure 9 Pressure loss versus mass flow rate for bare wafers, hot flow

TEST RESULTS

Effect of temperature: single layer wafers

Cold flow test results are shown in Figure 7. Horizontal and vertical error bars show the measurement errors for mass flow rate and the pressure, respectively.

The maximum difference in pressure loss between wafers (samples #15 and #4) is around 13%. This is attributed to the wafer quality

variation. To account for the difference in air density between the tests, the pressure loss is plotted versus mean wall velocity in Figure 8. The difference in pressure loss between samples #15 and #4 reduces from 13% to 12%.

A selection of results of hot flow test results are presented in Figure 9 - Figure 11. The pressure loss varies linearly with mass flow rate and mean flow velocity (Figure 9, Figure 10). Figure 11 shows pressure loss dependence on the air temperature upstream of the wafer. In order to obtain a pressure drop at regularly spaced mass flow rate values, linear interpolation has been used to get values for required mass flow rates. The variation between different wafer samples is consistent with the cold flow testing results (e.g. Figure 7) for temperatures below 400°C. Maximum difference between pressure loss for different samples is around 5% for 0.2 g/s, 7% for 0.3 g/s and 12% for 0.4g/s and 0.5 g/s mass flow rates.

To assess the importance of non-dimensional parameters, the friction factor in pore conduits can be defined as

$$C_f = \frac{\Delta P}{0.5\rho U_{pore}^2} \times \frac{d_p}{w}, \quad (2)$$

where

$$U_{pore} = \frac{U}{\varepsilon} \quad (3)$$

is an estimated pore velocity. Here ε = 0.64 is the wafer porosity and $d_p \approx 17.5$ (μm) the nominal mean pore size. These values have been provided by the monolith manufacturer. Using the same reference value to define the pore flow Reynolds number:

$$Re_{pore} = \frac{U_{pore} d_p \rho}{\mu} \quad (4)$$

results in a friction factor somewhat similar to the Darcy friction factor in a round pipe (Figure 12), although there is a considerable scatter of the data points due to the temperature effects for the same Reynolds number values.

Only one of the samples (#15) could be tested at temperatures up to 550°C because of the consistent wafer failure at temperatures above 450°C. This was caused by the high-temperature silicone sealer (rated up to 1000°C) failing to retain its flexibility. Although the results are not presented here because repeatability could not be demonstrated, they are encouraging and demonstrate that higher temperature testing is possible provided that a different sealant material is used.

Effect of layer number

For multilayer wafers, the flow is expected to follow a similar path for each layer, therefore it is reasonable to assume that the total loss will scale with the number of transverse walls the flow has to pass. This assumption has been confirmed by simple 2-dimensional CFD simulations (details not included here because the simulations have a setup very similar to that discussed below for single wafers). The two test samples were 4 cells thick, so that the flow had to cross 5 walls (Figure 4). To account for that, the total pressure loss was divided by 5.

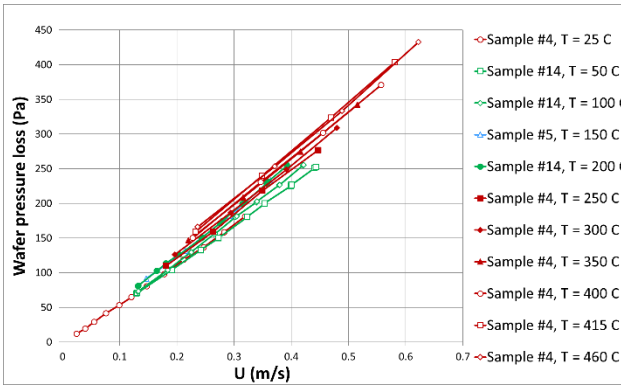

Figure 10 Pressure loss versus mean wall velocity for bare wafers, hot flow

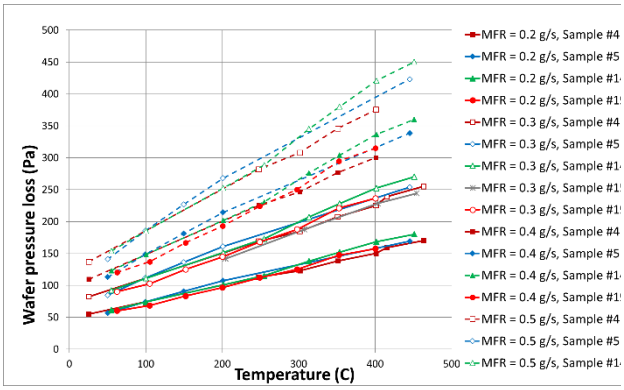

Figure 11 Pressure loss versus temperature for bare wafers, hot flow

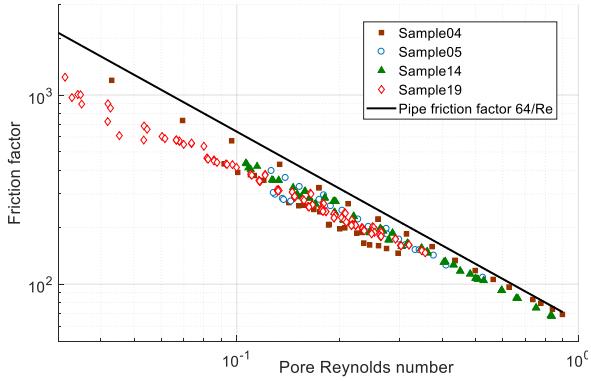

Figure 12 Friction factor versus pore Reynolds number

Comparison with the single layer wafer samples (Figure 13) shows that the total pressure loss through 5 walls is lower than the sum of pressure losses of individual layers. Only two cases are shown for single wafers, with the highest and the lowest pressure drops. The difference between the results for sample #15 and the multilayers samples is less than 10%. Since the multilayer wafers were cut from a different monolith, the variation between extrusions could be the cause of the discrepancy.

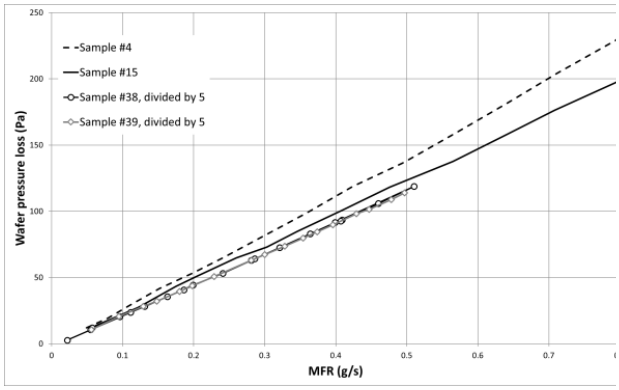

Figure 13 Comparison of pressure loss for single and multiple wafer samples, cold flow

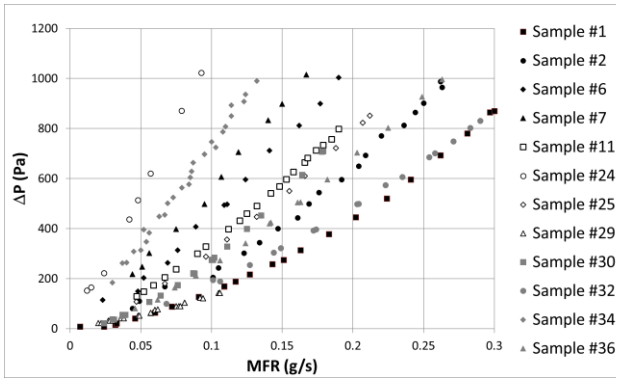

Figure 14 Pressure loss versus mass flow rate for coated wafers, cold flow

Effect of coating: single layer wafers

The test results for catalyst coated single layer wafers show the effect of coating variation on the pressure loss (Figure 14). Wafer coating analysis showed a significant difference between wafer samples depending on which part of the monolith they have been obtained. This indicates that single wafer testing is unsuitable for catalyst coated bricks, even if a wafer with even coating can be obtained from the manufacturer as used e.g. in [2], [19] and [18] - because of the manufacturing process the mean permeability of the walls of the full monolith will be very different to that measured. However, it is expected that multiple layer wafers may give more consistent results due to the averaging effect and will thus provide effective permeability. The method can also be applied to evaluate quality of coating and variability between different samples. This will be the subject of future work.

PERMEABILITY CALCULATION (COLD FLOW)

Permeability estimate

At very low flow velocities considered here inertial losses (such as contraction losses due to changes of cross-section area and Forcheimer losses) are negligible, therefore the total pressure loss can be approximated using Darcy law:

$$\Delta P = \frac{\mu}{k} U w \quad . \tag{5}$$

Here μ is the dynamic viscosity, U is the wall velocity, w is wall thickness and k is the permeability of the wafer. For the small pressure drops considered here, there is no need to account for density variation across the wafer. For a flat wafer of thickness w_0, expression (5) could be used directly to calculate the permeability of the cold flow using the mean wall velocity U_0:

$$k_0 = \frac{\mu}{\Delta P} U_0 w_0 \,. \tag{6}$$

On the other hand, because of the high resistance of the wafer to the flow in the thicker ridge areas, it can be assumed that no flow is going through the ridges so that

$$k_1 = \frac{\mu}{\Delta P} U_1 w_0 \,. \tag{7}$$

Here U_1 is the mean wall velocity assuming that only "flat" area of the wafer is available to the flow.

In reality, it is likely that some part of the flow will still flow through the ridged areas, therefore the real value of the wafer permeability will be between the two values described by equations (6) and (7).

The ratio of the "flat" area A_1 to the total area A_0 of the wafer is

$$\frac{A_1}{A_0} = \frac{d_h}{a} \,, \tag{8}$$

where a is the cell pitch and d_h is cell hydraulic diameter, therefore

$$\frac{k_1}{k_0} = \frac{a}{d_h} \,. \tag{9}$$

For a 300/8 monolith this ratio is around 0.86 (based on nominal hydraulic diameter value), so that choosing the average between the two:

$$k_2 = \frac{k_0 + k_1}{2} \,. \tag{10}$$

will result in an error within approximately 7%. While this is acceptable in some situations (for example, high mass flow rate conditions where the wall loss contribution may be lower than friction), a more precise estimate is possible as discussed in the CFD modelling section.

To estimate permeability k_0 from Eq. (6), linear regression analysis has been used for the pressure/velocity data sets presented in Figure 8. A similar analysis has been performed to obtain permeability k_1. The three permeability values described by Eqs. (6), (7) and (10) are shown for all wafer samples in Table 1. An alternative method for calculation of permeability (k_3) is introduced and discussed in the Ridge Correction section, but the values are presented here for convenience. The maximum variation in the permeability values between the wafers is 10% compared to the mean value.

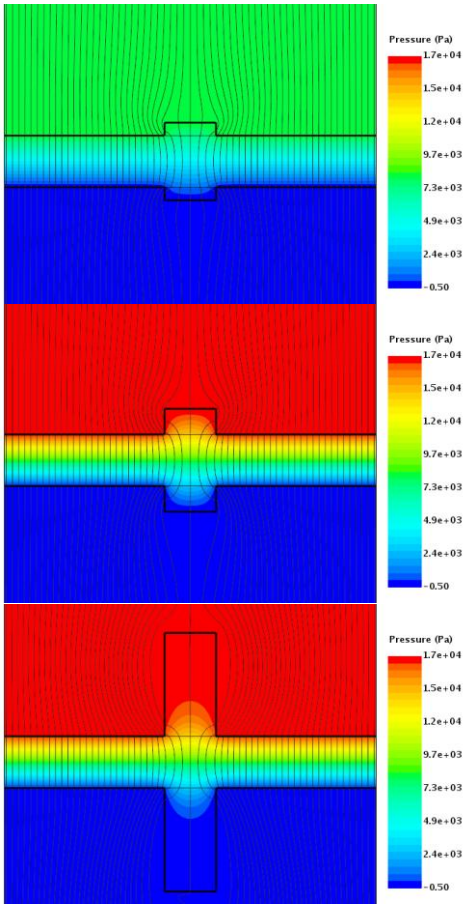

Figure 15 Flow streamlines for k = 1×10^{-13} m^2, 1.0 g/s mass flow rate and different ridge height (factors 0.25, 0.5 and 2 of wall thickness)

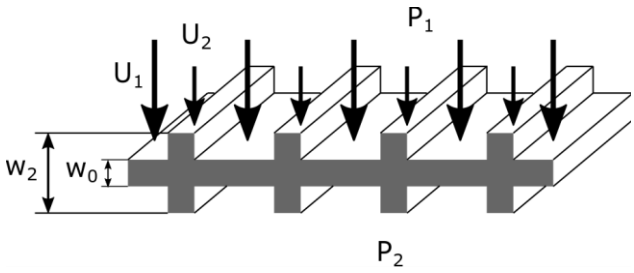

Figure 16 Schematic of flow through a wafer

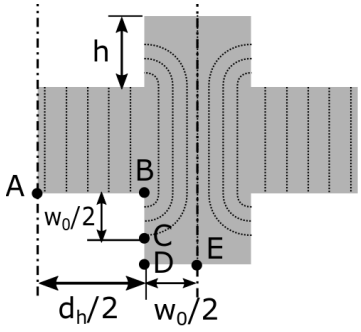

Figure 17 A schematic of streamlines used for permeability calculations

Table 1 Comparison of permeability calculated from experimental results using different methods and predictive models

	Wafer sample						
	#3	#4	#5	#14	#15	#16	#19
k_0 ($m^2\times10^{12}$)	5.99	5.64	5.89	6.13	6.45	5.86	6.73
k_1 ($m^2\times10^{12}$)	6.95	6.55	6.83	7.12	7.48	6.80	7.82
k_2 ($m^2\times10^{12}$)	6.47	6.09	6.36	6.63	6.96	6.33	7.27
k_3 ($m^2\times10^{12}$)	6.33	5.94	6.22	6.49	6.83	6.15	7.08

CFD modelling

Checking the validity of expressions (6), (7) and (10) is not feasible with the current experimental data, but CFD modelling can be used to estimate the effect of ridges of different height on the wafer pressure loss. Two-dimensional simulations have been performed in StarCCM+. The geometry is based on 300/8 bare wafer dimensions with periodic boundaries on both sides to replicate multiple channels (Figure 15) (note that only part of the inlet and outlet regions are shown in the figure). The length was chosen to ensure uniform flow at both inlet and outlet boundaries. Different ridge height is used, equal to $0.1w_0$, $0.25w_0$, $0.5w_0$, $0.75w_0$, $1.0w_0$ and $2.0w_0$. The flow is laminar with uniform flow velocity provided at the inlet, and atmospheric pressure assumed at the outlet boundary.

The porous wall was modelled using a porous medium approach [22]. Two permeability (k) values of 7×10^{-12} m^2 and 1×10^{-13} m^2 were used. The first one was chosen to be close to the permeability obtained for bare wafers, the second value is representative of the lowest permeability obtained for catalysed wafers, thus these values cover two limiting cases relevant to this study. These two ("nominal") values of k were used to define an extra source term in the Navier-Stokes equations:

$$S = \frac{\Delta P}{L} = \frac{\mu}{k}U \,. \qquad (11)$$

The total pressure loss ΔP across the wafer is calculated using average pressures at the inlet and outlet boundaries.

The permeability calculation results (Table 2) show that assuming uniform flow through all sections of the wafer (Eq. (6)) results in an underestimation of the permeability of around 4%. The assumption of no flow through ridge areas (Eq. (7)) results in an overestimation of the permeability by up to 12%. Using the average Eq. (10) results in error of approximately 4%.

Streamlines of the flow for different ridge heights (Figure 15) show that for higher ridges most of the flow enters the wafer through the flat section and sides of the ridge. The velocities through the top part of the ridge are very low. This is caused by the resistance from the porous medium being proportional to the flow velocity and the length of the air path through the wafer. Thus the air flow finds the shortest possible path through the wafer, avoiding the ridge where possible.

Table 2 Comparison of permeability calculated from modelling results using different methods

	Ridge height factor						
	0	**0.10**	**0.25**	**0.50**	**0.75**	**1.00**	**2.00**
Nominal permeability 7×10^{-12} m²							
k_0 ($m^2\times10^{12}$)	7.00	6.86	6.77	6.72	6.71	6.71	6.70
k_1 ($m^2\times10^{12}$)	7.00	7.96	7.85	7.80	7.79	7.78	7.78
k_2 ($m^2\times10^{12}$)	7.00	7.41	7.31	7.26	7.25	7.25	7.24
k_3 ($m^2\times10^{12}$)	7.00	7.75	7.41	7.11	7.10	7.10	7.10
Nominal permeability 1×10^{-13} m²							
k_0 ($m^2\times10^{13}$)	1.00	0.98	0.97	0.96	0.96	0.96	0.96
k_1 ($m^2\times10^{13}$)	1.00	1.14	1.12	1.12	1.12	1.12	1.12
k_2 ($m^2\times10^{13}$)	1.00	1.06	1.05	1.04	1.04	1.04	1.04
k_3 ($m^2\times10^{13}$)	1.00	1.11	1.06	1.02	1.02	1.02	1.02

Ridge correction

The modelling results indicate that most of the flow through the "ridge" enters at the side, turning inside and forming a nearly circle quadrant path before entering the main wafer section. A simplified model of the streamlines can be used as shown in Figure 17.

Assuming that the pressure is constant each side of the wafer surface, the Darcy law yields

$$\Delta P = const = \frac{\mu}{k} U(r)\, w(r)\,. \tag{12}$$

Here r is a position along the wafer/ridge surface, U(r) is the velocity of the flow entering at that point, and w(r) is the length of the corresponding streamline through the wafer.

Since the streamlines entering the ridge from the sides follow a nearly circular path, and there is negligible amount of flow entering the ridge through the top wall, the following coarse approximation of $w(x)$ can be used:

$$w(r) = \begin{cases} w_0 \ \text{ on interval AB} \\ w_0 + 2b \ \text{ on interval BC} \\ 0 \ \text{ on intervals CD and DE} \end{cases} \tag{13}$$

The points A, B, C, D and E are shown in Figure 17. Here b is a length of a quarter circle with radius equal to the distance from the flat wafer surface:

$$b(r) = \frac{\pi r}{2}\,. \tag{14}$$

Calculating mean velocity on the line ABCDE shown in Figure 17 gives

$$\frac{a}{2} U_0 = \int_{ABCDE} U(r)\, dr\,. \tag{15}$$

Using expressions (12) - (15) results in

$$\frac{a}{2} U_0 = \Delta P \frac{k}{\mu} \int_{ABCDE} \frac{1}{w(r)} dr = \Delta P \frac{k}{\mu} \left[\frac{d_h}{2w_0} + \int_0^{\min(h,\, w_0)} \frac{dr}{w_0 + \pi r} \right] =$$

$$= \Delta P \frac{k}{\mu} \left[\frac{d_h}{2w_0} + \frac{1}{\pi} \ln\left(\frac{2w_0 + \pi \min(h, w_0)}{2w_0} \right) \right]. \tag{16}$$

Thus, if the pressure loss is known, the permeability can be estimated as:

$$k_3 = \frac{a\mu}{2\Delta P} U_0 \times \left[\frac{d_h}{2w_0} + \frac{1}{\pi} \ln\left(\frac{2w_0 + \pi \min(h, w_0)}{2w_0} \right) \right]^{-1}. \tag{17}$$

For ridges higher than half the width of the wafer wall (which was the case for most of the wafers considered), the height of the ridge becomes irrelevant as negligible amount of air enters the ridge through its top part, and the permeability is equal to

$$k_3 = \frac{a\mu}{2\Delta P} U_0 \times \left[\frac{d_h}{2w_0} + \frac{1}{\pi} \ln\left(1 + \frac{\pi}{2} \right) \right]^{-1}. \tag{18}$$

As shown in Table 2, this expression gives values within 2% of the nominal permeability value for ridges equal or higher than half wall width which was the case for most wafers tested here. Although a more precise analysis is certainly possible, this accuracy is sufficient for the applications considered here.

Applying this method to the experimental data gives permeability values shown in Table 1 (k_3). Assuming (following the CFD analysis) that these values are more representative of the "true" permeability value, the mean value of $k_3 = 6.44\times10^{-12}$ (m^2) will be used as the reference for subsequent analysis.

Note that this correction has been developed for filters with constant wall thickness. However, a similar procedure can be employed for other filter configurations, for example, asymmetric filters with larger inlet channels, and appropriate correction can be readily developed using the method proposed here.

Predictive permeability models

Multiple empirical and phenomenological models exist allowing to estimate the porous wall permeability using its mean properties, such as porosity (ε) and pore size (d_p). Some of these have been reviewed by Dullien [13] with an unfortunate conclusion that the model performance depends critically on the various parameters such as pore shape, distribution, tortuosity factor etc. Experimental studies suggest that the expression for permeability will also be different for different porosity ratios. A selection of the most popular expressions is shown in Table 3. Plotting the ratio k / D^2 shows that in the range of porosities characteristic to DPFs and GPFs the difference between the models is considerable. For high porosities the difference between two popular models by Rumpf and Gupte and Carman-Kozeny is

Table 3 Predictive permeability models

Expression	Source
$k_5 = \frac{\varepsilon^3}{150(1-\varepsilon)^2} D^2$	Blake-Kozeny [13]
$k_6 = \frac{\varepsilon^3}{180(1-\varepsilon)^2} D^2$	Carman-Kozeny [13]
$k_7 = \frac{\varepsilon^{5.5}}{5.6} D^2$	Rumpf and Gupte [13]
$k_8 = \frac{2\left[2-1.8(1-\varepsilon)^{1/3}-\varepsilon-0.2(1-\varepsilon)^2\right]}{9(1-\varepsilon)} D^2$	Kuwabara [14]

Table 4 Comparison of permeability calculated using predictive models

	Based on d_p	Based on d_c
k_5 ($m^2 \times 10^{12}$)	4.13	8.15
k_6 ($m^2 \times 10^{12}$)	3.44	6.79
k_7 ($m^2 \times 10^{12}$)	4.70	9.27
k_8 ($m^2 \times 10^{12}$)	10.1	20.0

around 20%, while Kuwabara model gives values more than twice as high (Figure 19).

The characteristic dimension *D* can also be defined in different ways. Some authors use mean pore size, while others use the "equivalent circular tube diameter" defined as four times the ratio of the pore volume to the wetted surface area associated with a given sphere [13]:

$$d_c = \frac{2\varepsilon}{3(1-\varepsilon)} d_p , \quad (19)$$

which can result in more than 50% difference between d_c and d_p.

Permeabilities defined by expressions from Table 3 have been calculated using both pore size and d_c. The results are shown in Table 4 and vary considerably, thus confirming that each of the existing models is only suitable for a certain type of porous medium. Plotting these expressions against porosity (Figure 19) shows that the difference between the permeabilities calculated using these models increases with the porosity of the medium, i.e. will be more important for uncatalysed filters.

Multilayer wafers

Although the multilayer wafer samples give lower pressure loss (per single wall) when compared to the single wafers, the difference is within the 12% variation between samples seen for single wafers. The difference in pressure loss between the two tested multilayer samples is below 3% (Figure 13). This suggests that using multilayer wafers may give more consistent results as sensitivity to variability in wall property will be lower when averaging results from 5 walls. The values of permeability for samples #38 and #39 are $k_3 = 7.54 \times 10^{-12}$ (m^2) and $k_3 = 7.59 \times 10^{-12}$ (m^2), respectively. As the samples were cut from a different monolith, it was not possible to establish if the variation was caused by monolith variability, experimental error or other phenomena. However, the 10% error margin is still acceptable in some applications. Increasing number of layers should give better accuracy, however using thick samples presents some difficulties with sealing, therefore authors believe that 4-5 wall layers should be adequate.

PERMEABILITY CALCULATION (HOT FLOW)

Hot flow

The same procedure has been used to estimate the wafer permeability from the hot test results. For each temperature point, the permeability value was calculated by fitting the ridge-corrected expression (18) to the experimental data. The results are shown in Figure 20. It is apparent that the permeability value varies considerably with the temperature, which suggests that slip effect needs to be taken into account for hot flow at temperatures characteristic of gasoline engine exhaust gas.

Predictive slip models

The importance of slip effect is characterised by the value of the Knudsen number

$$Kn = \frac{\lambda}{D} , \quad (20)$$

where λ is the free mean path of the gas molecule and *D* is the characteristic length. Mean pore size d_p is often used as the characteristic length, while some authors (e.g. [4]) use characteristic dimension of a spherical collector instead, defined by Eq. (19). The mean free path can be defined as

$$\lambda = \frac{k_B T}{\sqrt{2}\pi\sigma^2 P} , \quad (21)$$

where $k_B = 1.3806 \times 10^{-23}$ (J/K) is Boltzmann constant, σ is the collision diameter and *P* is the pressure. The collision diameter can be assumed to be equal to the molecule diameter (around 4×10^{-10} m for air), or calculated from the known viscosity as

$$\sigma^2 = \frac{2\sqrt{m k_B T}}{3\pi^{3/2}\mu} . \quad (22)$$

Here *m* is the molecular mass of air ($m = 28.971 / N_A$ (g) with $N_A = 6.022 \times 10^{23}$). The two definitions of the collision diameter give different values (Figure 18) and this adds another layer of uncertainty to the definition of the Knudsen number.

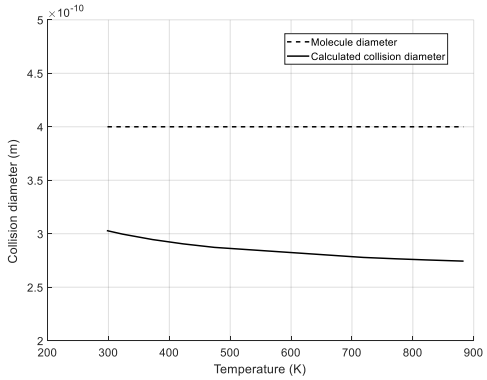

Figure 18 Molecule collision diameter

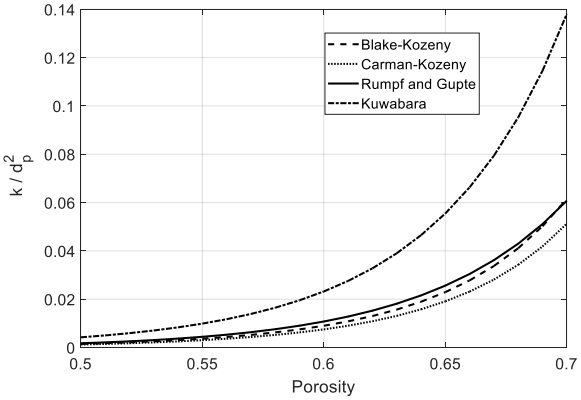

Figure 19 Comparison of predictive permeability models

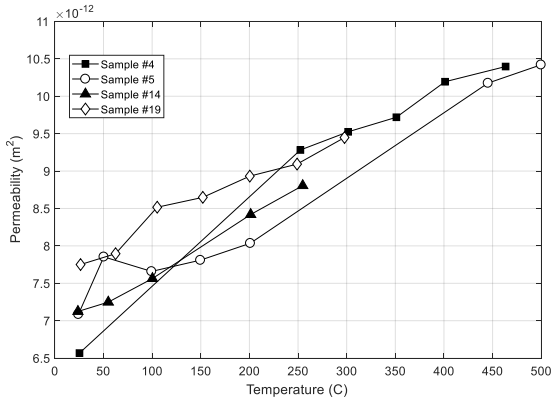

Figure 20 Permeability calculated from hot flow data

In the absence of experimental hot flow data, "predictive" slip models can be used to describe porous wall permeability at high values of Knudsen number ([4], [5]). Several such models exist.

The model suggested by Lee at al [23]:

$$k = \frac{2\left(K_1 + 3K_2\sigma Kn\right)}{9\left(1-\varepsilon\right)\left(1+2\sigma Kn\right)}\frac{d_c^{\,2}}{4} \tag{23}$$

with

$$K_1 = 2 - \frac{9}{5}\left(1-\varepsilon\right)^{1/3} - \varepsilon - \frac{1}{5}\left(1-\varepsilon\right)^2, \tag{24}$$

$$K_2 = 1 - \frac{6}{5}\left(1-\varepsilon\right)^{1/3} + \frac{1}{5}\left(1-\varepsilon\right)^2 \tag{25}$$

requires determination of σ, the Tangential Momentum Accommodation Coefficient. In most experiments conducted with air the values of TMAC have been shown to be close to 1 [25], although some other studies have produced lower values, e.g. Moghaddam and Jamiolahmady [24] report a value of 0.6.

Using value at *Kn* = 0 as the no slip permeability, one can then express

$$\frac{k}{k_0} - 1 = \frac{\left(K_1 + 3K_2\sigma Kn\right)}{\left(1+2\sigma Kn\right)K_1} - 1 = \sigma\, Kn\,\frac{3K_2 - 2K_1}{\left(1+2\sigma Kn\right)K_1}\,. \tag{26}$$

The model involving Stokes-Cunnigham Factor (SCF) described in [5] only requires a value of "continuum permeability" and Knudsen number:

$$\frac{k}{k_0} = SCF = 1 + Kn\left(1.257 + 0.4e^{-1.1/Kn}\right), \tag{27}$$

so that

$$\frac{k}{k_0} - 1 = Kn\left(1.257 + 0.4e^{-1.1/Kn}\right) \tag{28}$$

Slip correction

In order to evaluate the slip effect from the experimental results, permeability was calculated using Eq. (18) for all temperature points. The definition of collision diameter (22) is used for Knudsen number estimate, with pore size as the length scale.

Calculated permeabilities are plotted versus Knudsen number in Figure 21. Because of the scatter in the experimental data, an average of the 4 curves was calculated (shown by a dashed line) and used for further analysis. High temperature data for sample 5 are excluded from the analysis as no other measurements were available to confirm data validity.

Most existing slip models require knowledge of "no-slip" permeability. Generally speaking, cold flow permeability is not the same as no-slip permeability. Although only part of the data points lie in the full slip regime (Kn > 0.01), it is obvious from Figure 21 that even for cold flow (20°C) there is slip present. Bearing in mind the uncertainties of the Knudsen number definition, we follow the analysis presented in [24] and use extrapolation to find the non-slip permeability $k_0 = 6.07\times10^{-12}$ (m2). Non-dimensional plots (Figure 22) indicate that in the range of the Knudsen numbers considered the slip effect can be adequately described by a first order model:

$$k = k_0\left(1 + 4C_1 Kn\right). \tag{29}$$

Linear regression analysis for the averaged line yields slip coefficient $C_1 = 11.14$. This coefficient is often expressed in terms of Tangential Momentum Accommodation Coefficient σ_v (TMAC)

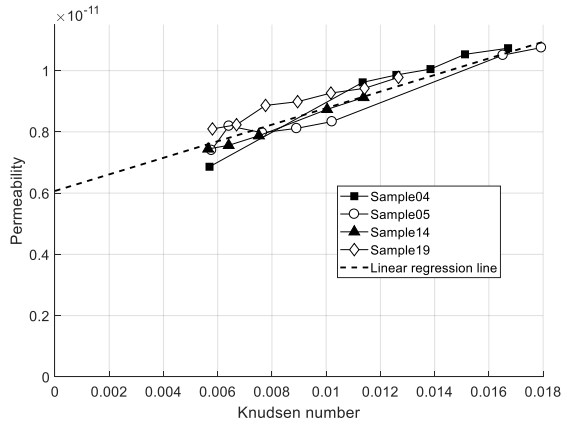

Figure 21 Permeability versus Knudsen number

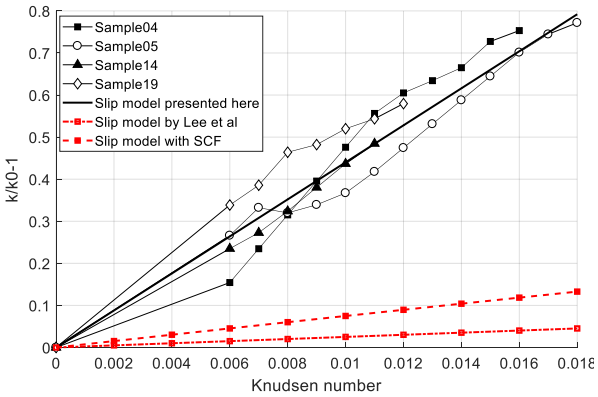

Figure 22 Comparison of different slip models

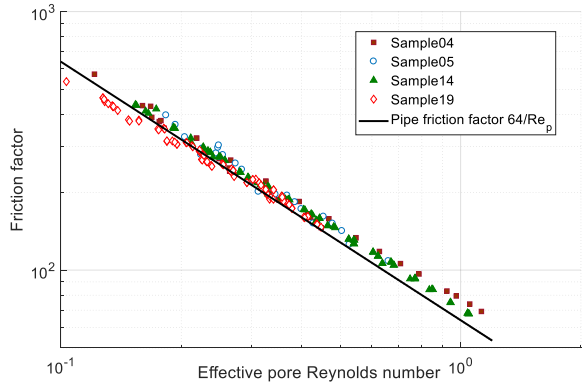

Figure 23 Friction factor versus pore Reynolds number

which characterises the tangential momentum transport between the gas and wall (see e.g. [25]):

$$\sigma_v = \frac{2}{C_1+1}. \tag{30}$$

This gives $\sigma_v = 0.1647$, which is low compared to the values of order 1 obtained in most other studies quoted in [25]. However, other authors have found lower TMAC values [24], therefore no clarity yet exists as to what values should be used for different surfaces and gases.

For practical applications, using temperature and pressure instead of Knudsen number is more convenient. Taking advantage of the fact that the mean free molecule path (as defined here) is proportional to $\mu\sqrt{T}$, the first order slip model can be rewritten as

$$k = k_0\left(1 + C\mu\sqrt{T}\right). \tag{31}$$

Note that dependence on pressure is not taken into account here as the pressure drop across the wafers was very low. With this definition, the corresponding slip coefficient can be found using linear regression as $C = 806.4$.

An alternative way to account for slip effect involves using effective viscosity instead of effective slip permeability [25]. Assuming that the Darcy losses can be expressed as

$$\Delta P = \frac{\mu_{eff}}{k_0} Uw, \tag{32}$$

the effective viscosity can be found as a function of Knudsen number. Using the fitting presented in Eq. (31), the effective viscosity can be approximated as

$$\mu_{eff} = \mu(T)\frac{k_0}{k_{slip}} = \frac{\mu}{1 + C\mu\sqrt{T}}. \tag{33}$$

This viscosity can be used to define the effective pore flow Reynolds number:

$$Re_{pore,eff} = \frac{U_{pore} d_p \rho}{\mu_{eff}}. \tag{34}$$

The resulting friction factor calculated from Eq. (2) is very close to the Darcy friction factor in a round pipe (Figure 23). The scatter of the data (compare with Figure 12) is significantly reduced.

Comparison of the permeability calculated from the experimental data with the existing predictive models (Figure 22) shows that these expressions considerably underestimate the slip effect. Thus, the apparent slip effect for filter wafers is more pronounced than that predicted by existing models.

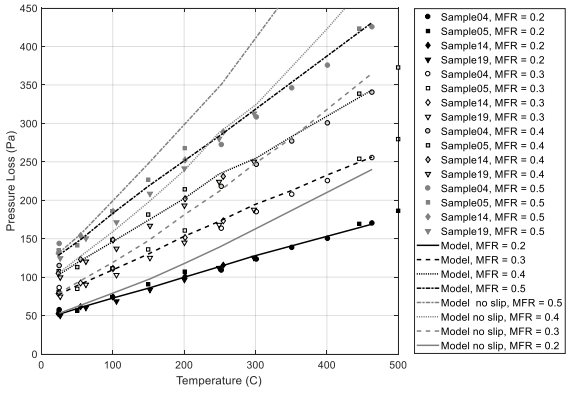

Figure 24 Comparison of experimental results to the model with and without slip

Slip model performance

To assess the importance of the slip effect, experimental results are compared with predictions using the Darcy formula (5) with and without slip correction (Figure 24). For higher temperatures, the error from the model without slip correction exceeds 40% for mass flow rates considered, while the maximum error for the model including slip is below 10% for the whole range of temperatures and mass flow rates for all samples. The error is highest for lower temperatures, and is within 5% for temperatures above 200°C. This means that the proposed model correctly addresses the high temperature effects, and thus offers a significant improvement to the existing models.

CONCLUSIONS

A new method for testing wafer samples and determining porous wall permeability for particulate filters has been developed and applied to several filter wafer samples. Moreover, a method for obtaining wafer samples from a monolith has been suggested, which is important because custom-made wafer samples are not readily available. The drawback of the method is the uneven surface of the wafers ("ridges") resulting from the wafer preparation process. In this work, we present a method that can be combined with the Darcy equation to correct the permeability estimation to account for the presence of these ridges, as shown in Eq. (18). Interestingly, it was found that having samples with higher "ridges" (of height more than half the wall thickness) results in improved accuracy, which makes sample preparation easier.

There are several limitations associated with this method. The method was not suitable for available coated wafer samples because of the significant variability of coating between different parts of the monolith. Achieving temperatures higher than 450°C has also proved challenging, as in this study the silicone sealant disintegrated at these temperatures. However, no other obstacles to obtaining higher temperature results were identified, and with a more suitable sealant higher temperatures can be achieved.

The permeability values estimated for the seven samples tested varied by a maximum of 10% from the mean value. This can be attributed to (a) measurement errors - mostly because of the limitations of the viscous flow meter used, and (b) sample to sample variation due to the different ridge heights: although the analysis shows that higher ridges would produce better results with the correction, this was not known at the testing stage and ridge height (average around 1 and 2 wall thickness values) was smaller in some areas of the samples. The standard error in the permeability values from the seven samples is ±2.5% of the mean, yielding $k = (6.44 \pm 0.15) \times 10^{-12}\ m^2$.

Some multi-layer wafer testing has been performed to explore the method's potential for permeability calculations. Although it was expected that the losses could be linked to the single layer results by a simple scaling factor, the total loss for multilayer samples was lower than expected. As this could have been caused by the variability between monoliths used for single and multiple layer testing, a firm conclusion could not be reached. However, the observed 10% difference between multilayer and single layer wafer results can still be acceptable in some cases.

Hot flow testing demonstrated the importance of the slip effect at the high temperatures characteristic of the gasoline engine exhaust systems, and a procedure for determination of the slip coefficient has been shown to provide good results for flow temperatures up to 450°C. A first order slip correction has been shown to be sufficiently accurate for the flow regimes considered. It is possible that a first order slip model is valid in the whole GPF operational temperature range so that a single slip coefficient is needed, however further testing would be beneficial. The slip coefficient is 5-10 times higher than the values predicted by some of the existing empirical models (23) and (27), which means that hot flow permeability correction is key in the development of a robust pressure loss model for high temperature flows. It has been demonstrated that higher temperatures (550°C) can be achieved if a better sealant is found for high temperature testing, this is the subject of ongoing work.

The relative error between the experiments and the proposed model is under 10% for the whole range of experimental data points for temperatures up to 450°C, with highest errors at lower temperatures (relative error is below 5% for all samples for temperatures above 200°C). To our knowledge, this is the first model providing such accuracy for a wide and realistic range of temperatures and mass flow rates.

In summary, the presented method allows to estimate both cold flow and hot flow permeability from samples easily prepared from a whole monolith. A distinct advantage of wafer testing compared to the whole monolith/core testing is that it eliminates additional uncertainties associated with other losses in the system (contraction/expansion and friction) and therefore provides more reliable values that can be used for material characterisation and developing models for predicting pressure losses in particulate filters.

The permeability values and slip corrections obtained from wafer samples can be used for predicting pressure loss in Diesel and Gasoline Particulate Filters, which is the topic of future research.

ACKNOWLEDGMENTS

We would like to thank the very thorough reviewers for their helpful comments and suggestions which helped improve the paper.

REFERENCES

[1] Johnson, T., "Vehicular Emissions in Review," SAE Technical Paper, 2013, 2013-01-0538, doi:10.4271/2013-01-0538.

[2] Lambert, C., Chanko, T., Dobson, D. and Pakko, J., "Gasoline Particle Filter Development," Emissions Control Science and Technology 3: 105-111, 2017, doi:10.1007/s40825-016-0055-x.

[3] Bissett, E.J., "Mathematical Model of the Thermal Regeneration of a wall-flow monolith diesel particulate filter," Chemical Engineering Science 39: 1233-1244, 1984, doi:10.1016/0009-2509(84)85084-8.

[4] Konstandopoulos, A.G. and Johnson, H., "Wall-Flow Diesel Particulate Filters - Their Pressure Drops and Collection Efficiency," SAE Technical Paper 890405, 1989, doi:10.4271/890405.

[5] Konstandopoulos A.G., Kostoglou M., Skaperdas E.,Papaioannou E., Zarvalis D. and Kladopoulou E., "Fundamental Studies of Diesel Particulate Filters: Transient Loading, Regeneration and Ageing," SAE Technical Paper 2000-01-1016, 2000, doi:10.4271/2000-01-1016.

[6] Konstandopoulos, A.G., Skaperdas, E. and Masoudi, M., "Inertial Contributions to the Pressure Drop of Diesel Particulate Filters," SAE Technical Paper 2001-01-0909, 2001, doi:10.4271/2001-01-0909.

[7] Konstandopoulos A.G.,"Flow Resistance Descriptors for Diesel Particulate Filters: Definitions, Measurements and Testing," SAE Technical Paper 2003-01-0846, 2003, doi:10.4271/2003-01-0846.

[8] Masoudi, M., Heible, A. and Then, P.M., "Predicting Pressure Drop of Wall-Flow Diesel Particulate filters - theory and experiment," SAE Technical Paper 2000-01-0184, 2000, doi:10.4271/2000-01-0184.

[9] Haralampous, G.A., Kandylas, I. P., Koltsakis, G.S. and Samaras, Z.C., "Diesel particulate filter pressure drop. Part 1: modelling and experimental validation," International Journal of Engine Research 5(2): 149-162, 2004, doi: 10.1243/146808704773564550.

[10] Opris, C.N. and Johnson, J.H., "A 2-D computational model describing the flow and filtration characteristics of a ceramic Diesel Particulate Trap," SAE technical Paper 980545, 1998, doi:10.4271/980545.

[11] Charbonnel, S. and Opris, C.N., "Fundamental Diesel Particulate Filter (DPF) Pressure Drop Model," SAE Technical Paper 2009-01-1271, 2009, doi:10.4271/2009-01-1271.

[12] Oxarango, L., Schmitz, P. and Quintard, M., "Laminar flow in channels with wall suction or injection: a new model to study multi-channel filtration systems," Chemical Engineering Science 59:1039-1051, 2004, doi:10.1016/j.ces.2003.10.027.

[13] Dullien, F.A.L,. "Porous media - Fluid Transport and Pore Structure," (Academic Press, New York, 1979), ISBN: 978-0-12-223651-8.

[14] Kuwabara, S., "The forces experienced by randomly distributed parallel circular cylinders or spheres in a viscous flow at small Reynolds numbers," Journal of the physical society of Japan 14:527-532, 1959, doi:10.1143/JPSJ.14.527.

[15] Watling, T.C., Ravenscroft, M.R., Cleeton, J.P.E., Rees, I.D. and Wilkins, D.A.R., "Development of a Particulate Filter Model for the Prediction of Backpressure: Improved Momentum Balance and Entrance and Exit Effect Equations," SAE Technical Paper 2017-01-0974, 2017, doi:10.4271/2017-01-0974.

[16] Koltsakis, G., Haralampous, O., Depcik, C. and Ragone, J.C., "Catalyzed diesel particulate filter modeling," Reviews in Chemical Engineering 29(1): 1–61, 2013, doi:10.1515/revce-2012-0008.

[17] Viswanathan, S., Rothamer, D., Zelenyuk, A., Stewart, M. and Bell, D., "Experimental investigation of the effect of inlet particle properties on the capture efficiency in an exhaust particulate filter," Journal of Aerosol Science 113:250-264, 2017, doi:10.1016/j.jaerosci.2017.08.002.

[18] Wirojsakunchai, E., Kolodziej, C., Yapaulo, R., and Foster, D., "Development of the Diesel Exhaust Filtration Analysis System (DEFA)," SAE Int. J. Fuels Lubr.1(1): 265-273, 2009, 10.4271/2008-01-0486.

[19] Yapaulo, R.A., Wirojsakunchai, E., Orita, T., Foster, D.E., Akard, M., Walker, L.R. and Lance, M.J., "Impact of filtration velocities and particulate matter characteristics on diesel particulate filter wall loading," International Journal of Engine Research 10:287-304, 2009, doi:10.1243/14680874JER03509.

[20] Martirosyan, K.S., Chen, K. and Luss, D., " Behavior features of soot combustion in diesel particulate filter," Chemical Engineering Science 65:42-46, 2010, doi:10.1016/j.ces.2009.01.058.

[21] Kamp, C.J., Zhang, S., Bagi, S., Wong, V., Monahan, G., Sappok, A. and Wang, Y., "Ash Permeability Determination in the Diesel Particulate Filter from Ultra-High Resolution 3D X-Ray Imaging and Image-Based Direct Numerical Simulations," SAE Int. J. Fuels Lubr. 10(2):608-618, 2017, doi:10.4271/2017-01-0927.

[22] Benjamin, S.F. and Roberts, C.A., "Methodology for modelling a combined DPF and SCR catalyst with the porous medium approach in CFD," SAE International Journal of Engines 7(4):1997-2011, 2014, doi:10.4271/2014-01-2819.

[23] Lee, K. W., Reed, L. D. and Gieseke, J. A., "Pressure drop across packed bed in the low Knudsen number regime," Journal of Aerosol Science 9:557-565, 1978, doi:10.1016/0021-8502(78)90021-6.

[24] Moghaddam, R. N. and Jamiolahmady, M., "Slip flow in porous media," Fuel 173:298-310, 2016, doi:10.1016/j.fuel.2016.01.057.

[25] Zhang, W.M.., Meng, G. and Wei, X., "A review on slip models for gas microflows," Microfluid Nanofluid 13:845-882, 2012, doi:10.1007/s10404-01-1012-9.

DEFINITIONS/ABBREVIATIONS

DPF	Diesel Particulate Filter
GPF	Gasoline Particulate Filter
MFR	Mass Flow Rate
SCF	Stokes-Cunnigham Factor
SCRF	Selective Catalytic Reduction Filter
TMAC	Tangential Momentum Accommodation Coefficient
VFM	Viscous Flow Meter